Use of intermediate focus for grazing incidence small and wide angle x-ray scattering experiments at the beamline P03 of PETRA III, DESY

9 AUTHORS, INCLUDING:

Adeline Buffet

Morpho Detection, SAFRAN group

54 PUBLICATIONS   **500** CITATIONS

SEE PROFILE

U.W. Gedde

KTH Royal Institute of Technology

278 PUBLICATIONS   **4,486** CITATIONS

SEE PROFILE

Mikael S Hedenqvist

KTH Royal Institute of Technology

186 PUBLICATIONS   **2,346** CITATIONS

SEE PROFILE

Stephan V Roth

Deutsches Elektronen-Synchrotron

363 PUBLICATIONS   **3,264** CITATIONS

SEE PROFILE

Use of intermediate focus for grazing incidence small and wide angle x-ray scattering experiments at the beamline P03 of PETRA III, DESY

G. Santoro, A. Buffet, R. Döhrmann, S. Yu, V. Körstgens, P. Müller-Buschbaum, U. Gedde, M. Hedenqvist, and S. V. Roth

Articles you may be interested in

Note: Comparison of grazing incidence small angle x-ray scattering of a titania sponge structure at the beamlines BW4 (DORIS III) and P03 (PETRA III)
Rev. Sci. Instrum. 83, 106104 (2012); 10.1063/1.4758285

Note: Grazing incidence small and wide angle x-ray scattering combined with imaging ellipsometry
Rev. Sci. Instrum. 83, 076107 (2012); 10.1063/1.4738880

Grazing incidence wide angle x-ray scattering at the wiggler beamline BW4 of HASYLAB
Rev. Sci. Instrum. 81, 105105 (2010); 10.1063/1.3488459

Present Status of BL40B2 and BL40XU at SPring8 (Beamlines for Small Angle Xray Scattering)
AIP Conf. Proc. 705, 336 (2004); 10.1063/1.1757802

High-pressure instrument for small- and wide-angle x-ray scattering. II. Time-resolved experiments
Rev. Sci. Instrum. 70, 1540 (1999); 10.1063/1.1149621

Use of intermediate focus for grazing incidence small and wide angle x-ray scattering experiments at the beamline P03 of PETRA III, DESY

G. Santoro,[1] A. Buffet,[1] R. Döhrmann,[1] S. Yu,[1] V. Körstgens,[2] P. Müller-Buschbaum,[2] U. Gedde,[3] M. Hedenqvist,[3] and S. V. Roth[1]

[1]*Photon Science, Deutsches Elektronen-Synchrotron DESY, Notkestr. 85, D-22607 Hamburg, Germany*
[2]*Physik-Department, Technische Universität München, Lehrstuhl für Funktionelle Materialien, James-Franck-Str. 1, D-85748 Garching, Germany*
[3]*KTH Royal Institute of Technology, School of Chemical Science and Engineering, Fibre and Polymer Technology, SE-10044 Stockholm, Sweden*

We describe the new experimental possibilities of the micro- and nanofocus X-ray scattering beamline P03 of the synchrotron source PETRA III at DESY, Hamburg (Germany), which arise from experiments with smaller beam sizes in the micrometer range. This beamline has been upgraded recently to perform new kinds of experiments. The use of an intermediate focus allows for reducing the beam size of microfocused hard X-rays while preserving a large working distance between the focusing elements and the focus position. For the first time, this well-known methodology has been employed to grazing incidence small- and wide-angle X-ray scattering (GISAXS/GIWAXS). As examples, we highlight the applications to *in situ* studies using microfluidic devices in GISAXS geometry as well as the investigation of the crystallinity of thin films in GIWAXS geometry. © *2014 AIP Publishing LLC*. [http://dx.doi.org/10.1063/1.4869784]

I. INTRODUCTION

The beamline P03/Micro- and Nanofocusing X-ray Scattering (MiNaXS)[1] provides a versatile platform for advanced X-ray scattering experiments. The optical design has been optimized for wide-, small-, and ultra-small-angle X-ray scattering in both, transmission and grazing incidence geometries. The range of applications covers investigations of thin films, organic photovoltaics, electronics, as well as microfluidics and material testing, e.g., deformation. In particular, the ability to observe devices *in operando* and the growth of nanostructures *in situ* is of great interest in materials science.[2,3]

In order to be able to characterize the desired structures and morphologies from the molecular level to the large scale domain structures, it is essential to allow for a combination of microfocusing optics and small- or wide-angle scattering in transmission or grazing incidence geometry.[4] We extend the capabilities of the beamline P03 with such a combination. We especially introduce a strategy to reduce the beam size at the sample position, while preserving a large working distance. This methodology is based on the production of an intermediate focus between the source and the sample and the subsequent refocusing of the X-ray beam at the sample position using two sets of beryllium compound refractive lenses (CRLs). This methodology is well known to be used in micro-diffraction.[5–7] We introduced this concept of intermediate focus for the first time to the combination of a microfocus with grazing incidence small- and wide-angle X-ray scattering (GISAXS/GIWAXS).[8]

The paper is structured as follows. First, we give a general, short overview over the different possibilities to provide focused X-ray beams. Then, we describe the installation of the intermediate focus at the beamline P03. Next, we give a brief layout of the SAXS/WAXS setup. Finally, we present three examples, which show the new capabilities of this combination: (1) scanning laterally colloidal layers in transmission geometry, (2) *in situ* investigation of structural changes during nanoparticle deposition in a microfluidic channel probed in grazing incidence geometry, and (3) determination of crystalline phases in thin polymer films probed as well in grazing incidence.

II. FOCUSING HARD X-RAY OPTICS

There exist several different optical elements to provide a focused beam in the hard X-ray regime using reflective, diffractive, or refractive optics, each with its specific advantage.[9,10] Among them, probably the most commonly used in beamlines worldwide are reflective mirrors in a Kirkpatrick-Baez arrangement.[11] The mirrors can be either static, i.e., mirrors polished to the desired profile for a given incidence angle and focus, or dynamic, i.e., flat mirrors that can be bent to the desired shape by actuators.[12] To enhance the reflectivity of the mirrors it is possible to use Bragg multilayer mirrors, where the reflected radiation at the interfaces of the multilayer is added coherently generating a considerable increase in reflectivity.[13] Mirrors possess several advantages, such as the non-dispersive focusing nature (not in the case of multilayer mirrors) and large acceptance, but their surface quality needs to be carefully controlled to achieve the best focusing capabilities.

Other kind of reflective optical elements that rely on total external reflection are capillaries.[14] In this case, the X-rays are reflected in the internal surface of a hollow tube and focusing capabilities are shown when the capillary is tapered. X-ray capillaries exhibit an intrinsic achromatic focusing capability,

as mirrors do. Nevertheless, the focal distance of these focusing elements is very short, allowing very stable operation but restricting the space for possible sample environments, which limits its use.

Similar to capillary optics, waveguides confine the X-rays within a low absorption material that is enclosed between two thin films with smaller refractive index.[15] For particular grazing incidence angles, a resonator effect takes place inside the waveguide, and the radiation exits the waveguide with an enhanced intensity. Waveguides can provide coherent beams, but, as for capillary optics, a highly accurate and precise alignment of both the beam and the sample is necessary. Moreover, their short focal distance limits the accessible sample setups and environments as well.[16]

Diffractive optics can also be employed for focusing hard X-rays using the so-called Fresnel Zone Plates (FZPs).[17] They are capable of focusing monochromatic light by the constructive interference of the wavefront, which is modified when passing through the zone plate. They consist of a series of concentric rings or one-dimensional (1D) line gratings whose width becomes narrower towards the outer end. One advantage of FZPs is their increased focal distance, allowing, e.g., for grazing incidence setups.[18] Their resolution is determined by the width of the outermost line and with the present lithographic techniques resolutions in the order of tens of nm are achievable. On the other hand, the focusing efficiency of FZPs, i.e., the fraction of incident photons that become diffracted at the focus, depends on the height of the structure and higher structures are required as the energy of the X-rays is increased.[19] This implies that in the hard X-ray regime it is necessary to fabricate structures with extreme aspect ratios (height/width of the narrower zone),[20] which is difficult by lithographic techniques. In order to surpass this problem, Multilayer Laue Lenses (MLLs) have been developed.[21,22] They are linear zone plates fabricated by thin film deposition methods and subsequent sectioning and thinning. Therefore, aspect ratios in the range from 10^3:1 to 10^4:1 can be realized enabling an enhanced efficiency.

Lenses based on refractive optics for X-rays are nowadays one of the most popular X-ray focusing devices at synchrotrons worldwide.[23–25] Like FZPs, they work on axis providing an easy alignment and operation, and they present a good stability. Since the real part of the refraction index in the X-ray region is lower than 1, they must have a concave shape and the use of low atomic number (low-Z) materials, such as Al or Be, for their fabrication reduces significantly the

absorption of radiation.[26] It is possible to use arrays of concave lenses – the so-called Compound Refractive Lenses (CRLs) – to achieve reasonable focus distances. It is also possible to use lenses with two-dimensional (2D) focusing capabilities or two sets of 1D focusing lenses in a Kirkpatrick-Baez configuration.[27] These last ones show a significant increase in photon flux as their shape can be easily optimized due to the easier production process.[28]

Regardless of the optical elements used for focusing, in general, smaller beams imply a considerable decrease of the focus distance. This fact limits the use of microfocused X-ray beams with special sample setups, e.g., cryostats,[29] sputter deposition chambers,[30–32] and molecular beam epitaxy chambers,[33] or the combination of different techniques with microfocused X-ray techniques, like the simultaneous measurement of imaging ellipsometry and microfocus grazing incidence X-ray scattering,[34,35] micro-Raman spectroscopy and transmission X-ray microdiffraction,[36] or dielectric spectroscopy and X-ray scattering.[37] In this sense, the development of strategies that can provide focused small micrometer- or submicrometer-sized beams with large working distances is of great interest.

III. INTERMEDIATE FOCUSING METHODOLOGY

In Fig. 1, three images recorded at the sample position using an X-ray energy of 13.0 keV are shown. The images were recorded with a SESO X-ray beam monitor (Société Européenne de Systèmes Optiques, France) with a pixel size of (7.4×7.4) μm^2 and a field of view of (5.8×4.9) mm^2. The distances from the first transfocator (CRL1) and the second transfocator (CRL2) to the sample position were 7920 mm and 3100 mm, respectively. In order to avoid damaging the X-ray beam monitor, all the images were acquired using a 0.5 mm Al foil and a 0.1 mm Ag foil to reduce the beam intensity. Fig. 1(a) shows the image obtained when only 2 pinholes were used at each CRL transfocator. Fig. 1(b) was recorded using 55 lenses and 2 pinholes at CRL1 ($N_1 = 55$). Since the intermediate beam focus is well before the sample position, the intensity is spread. The structures that can be seen in this picture correspond to the Al and Ag foils used as attenuators. When 29 lenses were used in CRL2 ($N_2 = 29$) to refocus the beam coming out from CRL1 (Fig. 1(c)), a highly focused beam was obtained.

In order to characterize the intermediate focus geometry, we measured the beam size at the intermediate focus position
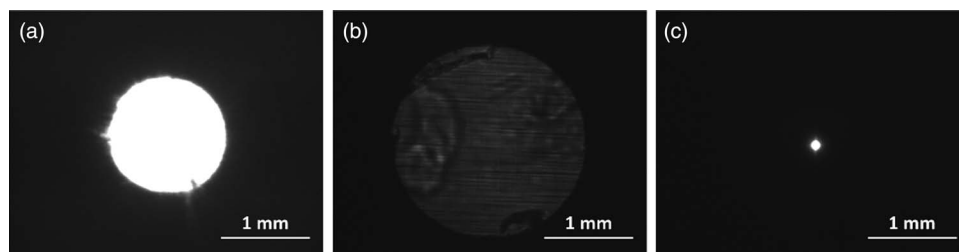

FIG. 1. Images recorded at 13.0 keV with a SESO X-ray beam monitor at the sample position for different lenses configurations. (a) CRL1: 2 pinholes; CRL2: 2 pinholes. (b) CRL1: 55 lenses + 2 pinholes; CRL2: 2 pinholes. (c) CRL1: 55 lenses + 2 pinholes; CRL2: 29 lenses + 2 pinholes. All the images were recorded using a 0.5 mm Al foil and a 0.1 mm Ag foil as beam attenuators.
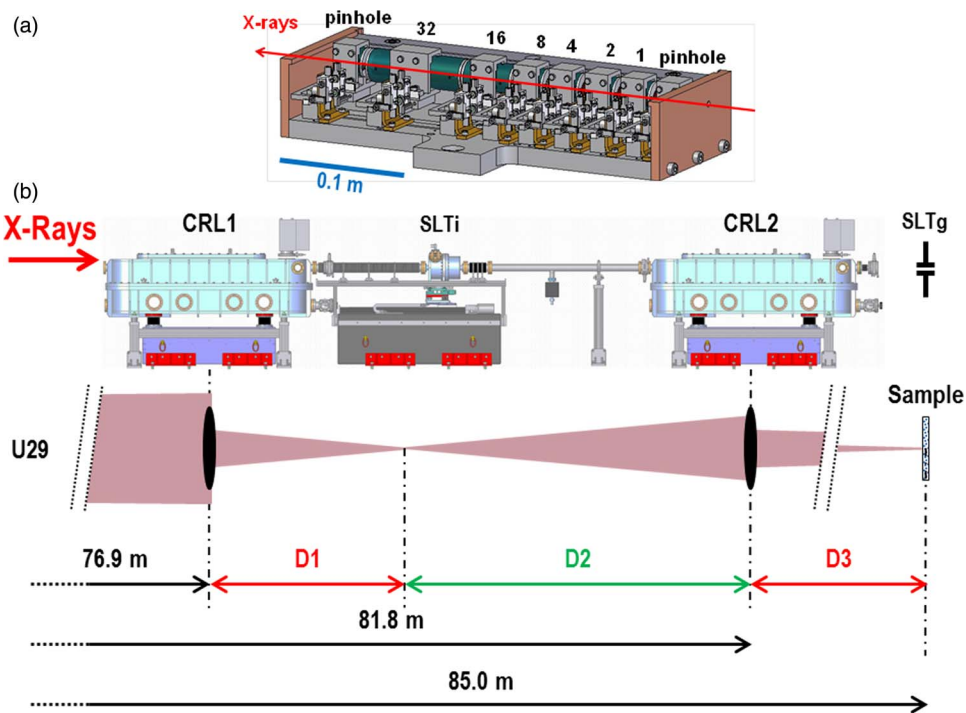
FIG. 2. (a) Sketch of the lenses transfocators available at the beamline. The number of lenses that each package comprises is indicated. (b) Schematic representation of the intermediate focusing methodology. The first set of lenses (CRL1) is located at 76.9 m from the undulator (U29) source, and it is employed to produce a focused beam at a distance D1 from CRL1 and at a distance D2 from the second transfocator (CRL2) that is used to refocus the beam at a distance D3 (sample position). SLTi denotes the slits system used for measuring the intermediate beam size while SLTg denotes the slits system used for the measurement of the beam size at the sample position. SLTi can be moved along the beam direction.

as a function of the distance from CRL1 ($D1$ in Fig. 2), i.e., we performed caustic measurements both for the horizontal and vertical beam profile and at two different photon energies, 11.4 keV (Fig. 3(a)) and 13.0 keV (Fig. 3(b)). The caustic measurements were fitted to hyperbolas (solid lines in Fig. 3). For a fixed energy of 11.4 keV and with $N_1 = 42$, a focusing distance $D1$ of 1280 mm was found and the associated beam size was (20.2×17.7) μm^2 (Horiz. $\times$ Vert.). Using 13.0 keV as photon energy and $N_1 = 55$, a beam size of (9.6×7.9) μm^2 (Horiz. $\times$ Vert.) at a focusing distance $D1$ of 950 mm was observed.

When CRL2 was used to refocus the intermediate focus at the sample position, smaller beam sizes were achieved. In Fig. 4, the knife-edge scans both for the horizontal and vertical directions and at the two different energies employed are shown.

In the case of 11.4 keV, the distances from CRL1 and CRL2 to the sample position were 7785 mm and 3075 mm, respectively. Using a number of lenses $N_1 = 42$ and $N_2 = 24$ a beam size of (12.7×10.8) μm^2 was achieved. Employing only CRL2 for focusing with $N_2 = 13$ a similar focus distance $D3$ of 3070 mm was obtained but the beam size for this configuration was (27.6×22.8) μm^2 (not shown). When the employed photon energy was 13.0 keV, a smaller beam was achieved using $N_1 = 55$ and $N_2 = 29$ lenses and placing the transfocators CRL1 and CRL2 at 7920 mm and 3100 mm from the sample position, respectively. In this case, a beam size of (6.9×4.8) μm^2 was measured. When only
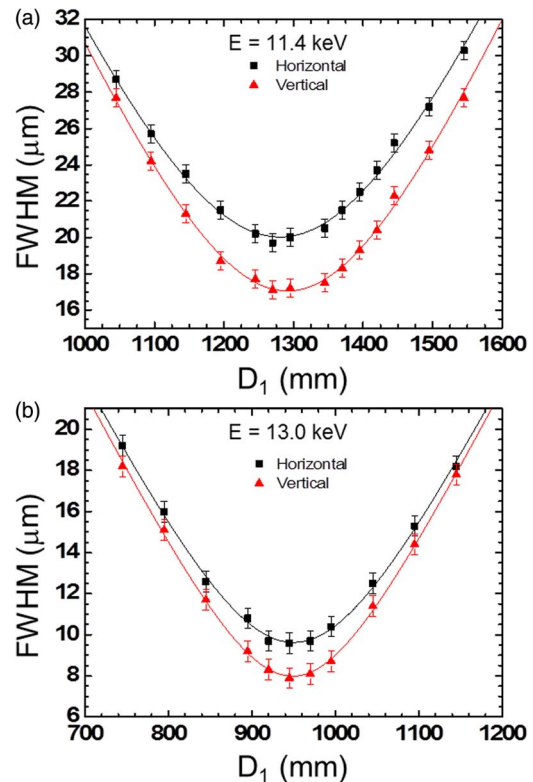

FIG. 3. Caustic measurements for the intermediate focus at a fixed energy of (a) 11.4 keV and (b) 13.0 keV. The solid lines are the hyperbolic fitting of the experimental data.
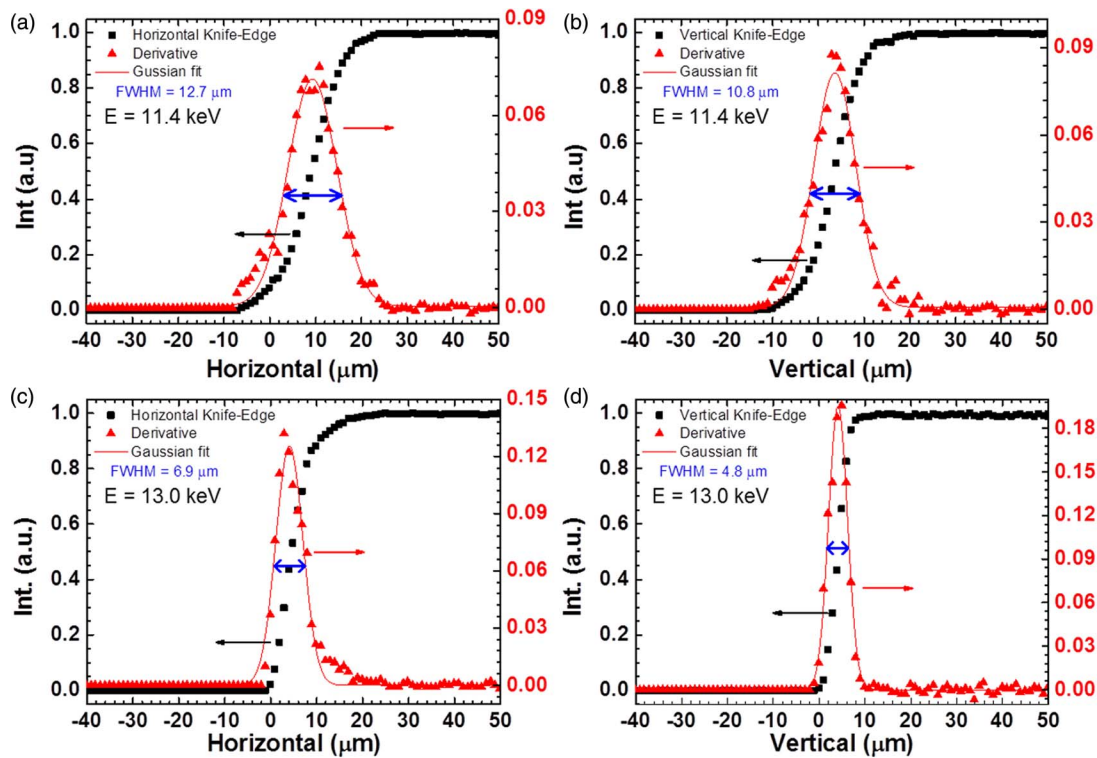
FIG. 4. Knife-edge scans of the refocused beam at the sample position at energies of 11.4 keV (a) and (b) and 13.0 keV (c) and (d). The CRL1 to CRL2 distances (D1+D2) were 4710 mm for 11.4 keV (N_1 = 42 and N_2 = 24) and 4820 mm for 13.0 keV (N_1 = 55 and N_2 = 29) and the focusing distance D3 from CRL2 was 3075 and 3100 mm for 11.4 keV and 13.0 keV, respectively. The full-width at half-maximum of the Gaussian fits is indicated by blue arrows.

CRL2 was used for focusing the X-rays at a photon energy of 13.0 keV and with a comparable working distance D3 of 3080 mm and N_2 = 16, the associated beam size was (22.8 × 17.2) μm^2 (not shown). All these results are summarized in Table I.

The abovementioned results imply that with the strategy employed in this work we have been able to decrease the beam size in more than 2 times for 11.4 keV and more than 3 times for 13.0 keV while maintaining the same focus distance. In practice, this turns into having access to smaller beams with the same working distance, i.e., there is enough space available for coupling the microfocused beam

to special sample setups or for the combination with other techniques.

IV. THE (GI)SAXS/(GI)WAXS SETUP OF MiNaXS

Fig. 5 shows a sketch of the standard setup for (GI)SAXS/(GI)WAXS at P03. The newly installed WAXS device consists of a flexible holder for the 2D WAXS detector. The 2D detector is typically a PILATUS 300k or 1M (Dectris Ltd., Switzerland) due to its high signal-to-noise ratio. The whole WAXS device is placed on air pads, thereby allowing flexible positioning in the hutch to adjust

TABLE I. Focusing configurations with and without prefocusing.

E^a (keV)	$N_1{}^b$	$D1^c$ (mm)	$D2^d$ (mm)	$N_2{}^e$	$D3^f$ (mm)	H^g (μm)	V^h (μm)
11.4	…	…	…	13	3070 ± 2	27.6 ± 0.2	22.8 ± 0.2
11.4	42	1280 ± 2	3430 ± 2	24	3075 ± 2	12.7 ± 0.2	10.8 ± 0.2
13.0	…	…	…	16	3080 ± 2	22.8 ± 0.2	17.2 ± 0.2
13.0	55	950 ± 2	3870 ± 2	29	3100 ± 2	6.9 ± 0.2	4.8 ± 0.1

[a]X-ray energy.
[b]Number of lenses at CRL1.
[c]Distance from CRL1 to the intermediate focus position.
[d]Distance from the intermediate focus position to CRL2.
[e]Number of lenses at CRL2.
[f]Distance from CRL2 to the focus at the sample position.
[g]Horizontal beam size at the sample position.
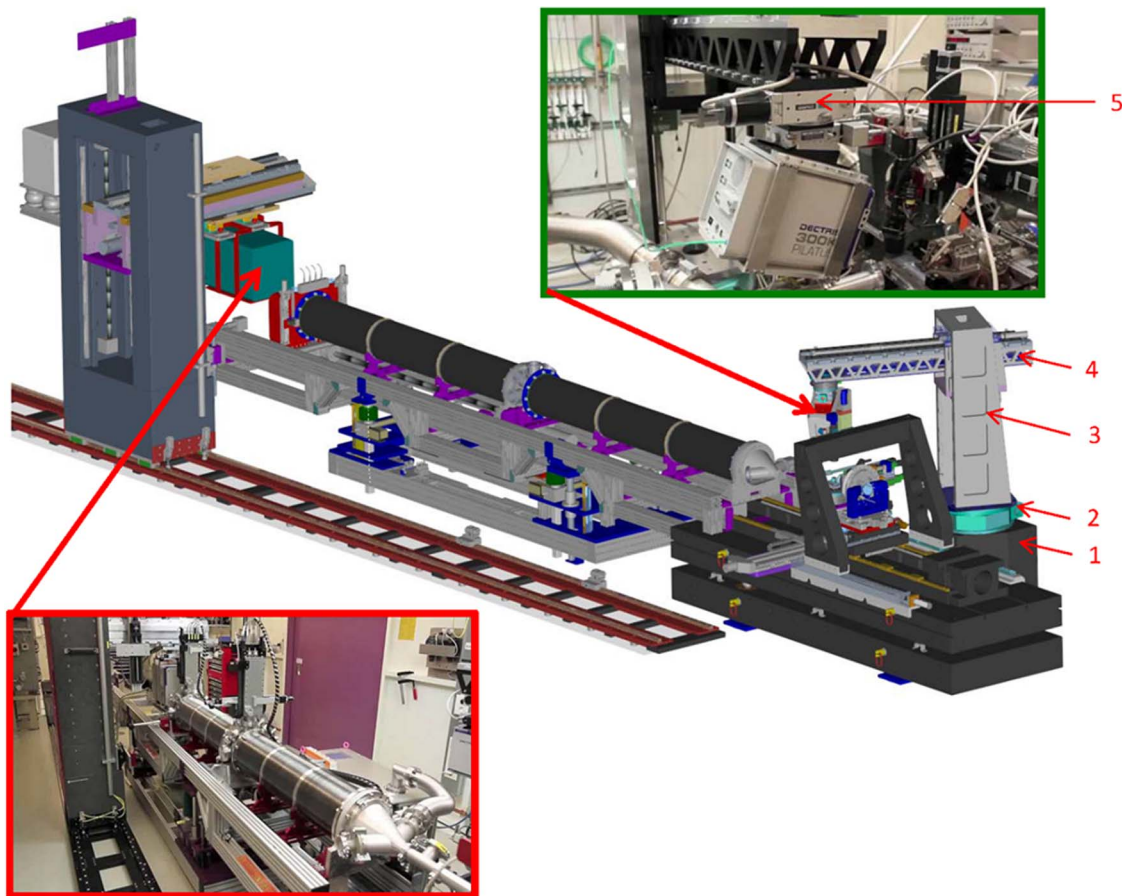[h]Vertical beam size at the sample position.

FIG. 5. Overview of the μ(GI)WAXS/(GI)SAXS setup at P03. 1 – Granite support on air pads, 2 – device rotation, 3 – vertical translation, 4 – horizontal translation, 5 – detector tilt and rotation.

the q-range. Two translational and three rotational axes allow for positioning the detector in space near the sample position.

V. SELECTED RESULTS

In order to demonstrate the measurement capabilities of the microfocused beam achieved with the intermediate focusing strategy, we present a selection of three different model cases.

A. Colloidal thin films

A sample consisting in polystyrene (PS) nanoparticles with a diameter of 100 nm (Kisker Biotech, Germany) solution-cast on top of a glass slide was measured in transmission geometry using SAXS. The sample to detector distance was 4909 ± 1 mm and the energy employed was 13.0 keV using the focusing configuration described in Sec. III for this energy, i.e., a beam size of (6.9×4.8) μm^2 (Horiz. $\times$ Vert.). A 2D detector Pilatus 300k was employed for acquiring the scattering patterns. Scattering from a neat glass slide was used as background.

Fig. 6(a) shows an optical microscope image of the sample. It can be clearly observed that there exist structures on the

dried solution-casted glass slide. These structures are related to the self-assembly and agglomeration of the PS nanoparticles during the drying process. One hundred scattering patterns were recorded in a line scan (along the red line in Fig. 6(a)) with a step size of 5 μm. The radial integration of the obtained scattering pattern at $d = 0$ μm is presented in Figure 6(b) together with the form factor of a sphere with a radius of 100 nm, showing a good agreement to each other.

Figs. 6(c) and 6(d) show the 2D scattering patterns recorded at $d = 125$ μm and at $d = 175$ μm, respectively. It can be clearly observed that at $d = 125$ μm an isotropic scattering ring was found while at $d = 175$ μm a powder-like scattering pattern was obtained. Fig. 6(e) shows the azimuthal integration map for the first order scattering peak, i.e., the intensity of the scattering peak with respect to the azimuthal angle for each spatial position, d. As the distance d increases, the scattering patterns transform from isotropic rings to powder-like scattering patterns.

This fact can be understood taking into account that the evaporation front direction from the solution-cast material is radial to the center. Therefore, in the outermost region the drying process occurred too fast preventing the PS nanoparticles to form homogeneous long-range ordered arrays.[38–40] In this region, weakly textured polycrystallites of PS spheres are present that are responsible for the powder-like scattering patterns.[41,42] On the other hand, in the inner part the
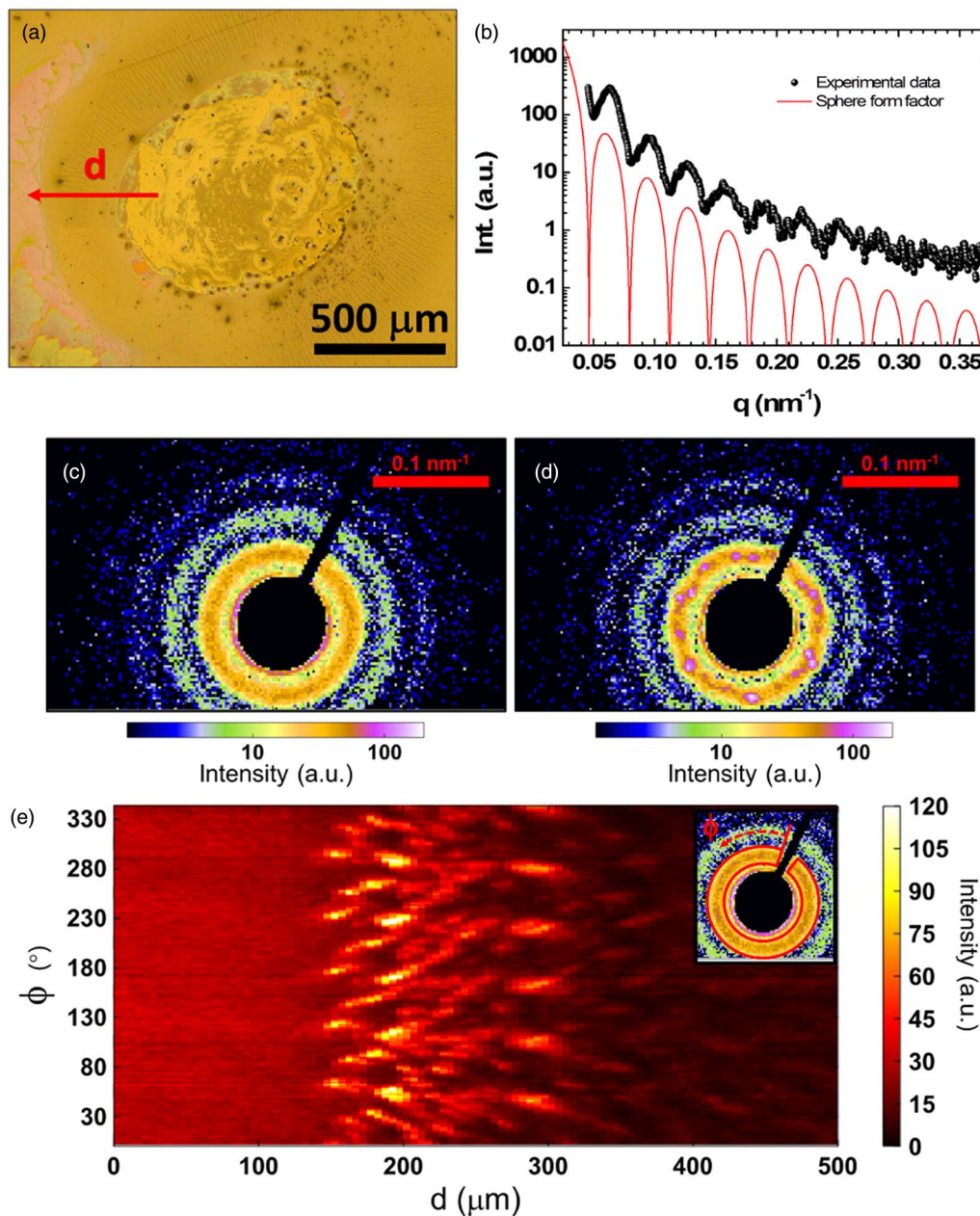
FIG. 6. (a) Optical microscopy image of the sample. The arrow indicates the direction of the scan, opposite to the evaporation front direction. (b) Radial integration of the scattering pattern at $d = 0$ μm. The solid line represents the form factor of a sphere with a radius of 100 nm. The curves are shifted for clarity. (c) Scattering pattern at $d = 125$ μm. (d) Scattering pattern at $d = 175$ μm. (e) Azimuthal integration map. The inset shows the azimuthal integration region on the scattering pattern at $d = 0$ μm.

evaporation is slow enough to allow the PS nanoparticles to self-assemble and, thus, the powder-like scattering patterns are not present but isotropic rings are found.[43,44] It is important to note that the region between the two different dried regions exhibits an extension of only 15 μm, implying that a beam size smaller than this value is needed in order to resolve the transition from one dried region to the other.

B. Microfluidics

With a special designed flow cell structural changes at the solid-liquid interface in microfluidic flow are accessible with GISAXS.[44–46] The beamline P03 facilitated the investigation of the swelling and structural changes in composite

films under laminar flow conditions.[47] The intermediate focused X-ray beam using the focusing configuration described in Sec. III for 13.0 keV is particularly suitable for the technique as it allows adapting the footprint of the incident beam to the width of the microfluidic channel. Thus, an extensive over-illumination of the sample not in contact with the fluid is prevented. In Fig. 7(a), the GISAXS geometry is shown together with a sketch of the microfluidic cell made out of cyclic olefin.[44,47] A side view is shown in Fig. 7(b). Two inlets are available for mixing experiments. However, in the example given, only one inlet was used for simplicity.

The experiment started with a dry polymer film of poly(ethyleneimine) (molecular weight $M_w = 750\,000$ g/mol, Sigma-Aldrich, Germany) on a silicon substrate. GISAXS
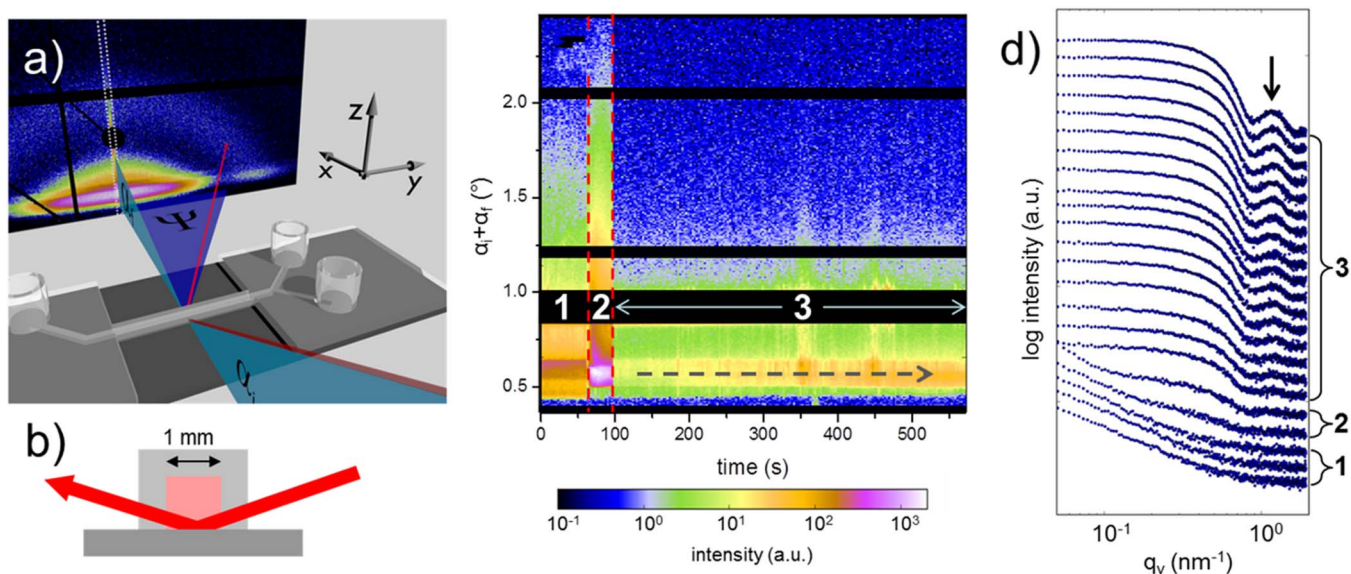
FIG. 7. (a) GISAXS setup with microfluidic cell, the incoming X-ray beam with the incident angle α_i is depicted in red. Scattered intensity with the exit angle α_f and the out of plane angle Ψ is recorded on a 2D detector. (b) Illustration of the X-ray beam transmitting the channel walls and the footprint on the sample surface; note that for clarity incident angle and X-ray beam are not in scale. (c) Composite image of vertical line profiles at $q_y = 0$ for 210 consecutive measurements scanning the microfluidic channel along y-direction while gold nanoparticles attach to a poly(ethyleneimine) thin film; regions in black correspond to the position of the specular beamstop and the inter-module gaps of the Pilatus detector; see text for numbers indicating different regimes in the microfluidic experiment. (d) Horizontal line profiles for *in situ* microfluidic experiment as sum of 10 consecutive measurements; intensity is shifted for clarity along intensity-axis with the initially dry film at the bottom.

data were collected with a 2D detector Pilatus 1M (Dectris Ltd., Switzerland) at a sample to detector distance of 2455 $\pm$ 1 mm. The incident angle α_i was 0.46°. In the investigation, the attachment of gold nanoparticles of 10 nm diameter out of aqueous dispersion (Cytodiagnostics, Canada) was studied. A flow of the gold nanoparticle solution with a flow speed of 0.02 ml/min was realized with a syringe pump (Nemesys, Cetoni, Germany). The microfluidic cell was moved perpendicular to the X-ray beam (along the y-axis, with X-ray beam oriented along the x-axis and the surface normal along the z-axis) with 50 μm steps opposed to the direction of the flow in the microfluidic channel. From the 2D GISAXS data 1D line profiles were extracted.

The course of the microfluidic experiment can be followed by combining vertical line profiles at $q_y = 0$ integrated over several pixels (box surrounded by dotted line in Fig. 7(a)) at different times into a composite image (see Fig. 7(c)). The vertical line profiles give structural information in the direction of the surface normal. Three different regimes can be distinguished in the composite image (separated by red dashed lines in Fig. 7(c)): (1) The scattering originating from the dry film, (2) scattering from a precursor of liquid which wets the surface, and (3) scattering in case the channel is completely filled and the attachment process of nanoparticles can be followed. The increasing intensity in the Yoneda peak is indicating the nanoparticle attachment (see grey dashed arrow in Fig. 7(c)).

Information about the lateral structure is given by horizontal line profiles (Fig. 7(d)). The increase in intensity of a peak originating from the form factor of spheres (marked with black arrow in Fig. 7(d)) is observable and shows the proceeding coverage of the polymer film with gold nanoparticles. For

clarity, the scattering curves of 10 consecutive measurements have been added up for the curves shown in Fig. 7(c). The numbers to the right of the curves in Fig. 7(d) correspond to the regimes of the microfluidic experiment as assigned in Fig. 7(c).

In general, the combination of microfluidic devices and GISAXS technique with the adapted intermediate microfocused X-ray beam allows for a multitude of investigations at the solid-liquid interface. Attachment and detachment processes, swelling and structural reorganization of thin films, as well as particle growth and mixing experiments under laminar flow conditions are accessible with this approach.

C. Crystallinity of poly(ε-caprolactone) (PCL) films

The lateral habit, unit cell structure, and melting behavior of single crystals of PCL prepared by the Rapid Expansion of a Supercritical Solution (RESS) technique was studied by AFM at ambient and higher temperatures and by GIWAXS at room temperature. GIWAXS was performed at a photon energy of 13.0 keV using the focusing configuration described in Sec. III. An incident angle of $\alpha_i = 0.5°$ and a sample to detector distance of 197.1 $\pm$ 0.1 mm were used.

After dissolving PCL in a solution of supercritical CO_2 and 0.1 vol.% chloroform, an extremely fast phase transfer from a supercritical to a gas-like state occurred during expansion into atmospheric conditions, leading to a temporary temperature drop to below -50 °C at the silica surface where the crystals were deposited. Single crystals of a hitherto unreported rectangular lateral habit were observed by AFM. Six-sided crystals were also observed, but they were fewer than the rectangular crystals and in addition the angles between
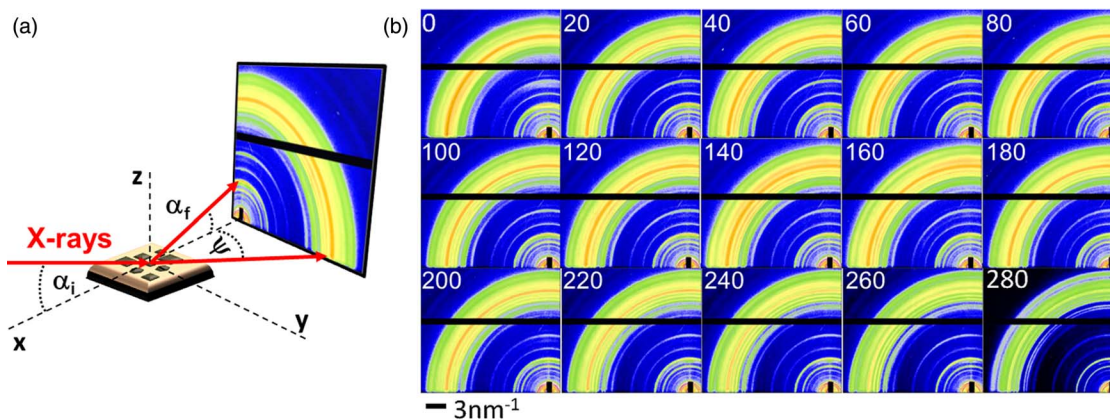
FIG. 8. (a) Sketch of the GIWAXS setup. The X-ray beam impinges on the polymer sample at an angle α_i. The scattered intensity at an angle α_f and out of plane angle Ψ is recorded on a 2D detector revealing the crystalline structure of unusual rectangular lateral habit single crystals in PCL. (b) Large area lateral scan (along the y direction) to check the crystalline homogeneity of the PCL sample installed by RESS. The scan step size was 20 μm. The numbers in each image indicate the scan position in μm. For a detailed analysis of the crystallinity, please refer to Ref. 48.

the lateral faces were different from the theoretical angles between adjacent {110} faces and {110} and {100} faces. X-ray scattering indicated a polymorphic structure also including the orthorhombic (110) and (200) diffraction peaks. Distinct low angle peaks essentially along the c-axis indicated a stacking on a very fine scale (3.7–4.7 nm) within the crystals. The equatorial diffraction peaks indicated a less dense packing of the PCL stems.

The unusual conditions for crystallization used gave the polymer molecules a severe limitation to rearrange from the initial random coil state. The facetted crystals consisted of a stack of 4 nm thick blocks; these blocks most probably constituted a regular variation in molecular packing, i.e., molecular order. The pronounced changes in the angles between adjacent faces from those observed in mature PCL crystals and the GIWAXS data indicated the presence of conformational disorder in the crystals.[48] Fig. 8 presents a sketch of the GIWAXS geometry together with the GIWAXS scattering patterns obtained from a lateral scan over the sample (along the y direction in Fig. 8(a)). The scan size was 280 μm using a step size of 20 μm. Although variations on the relative intensities of the scattering peaks were found, the main scattering peaks were present at every scanned position proving the overall homogeneity of the PCL crystalline structure installed by RESS (Fig. 8(b)).

VI. CONCLUSIONS

We have described new experimental capabilities of the beamline P03 at PETRA III. Driven by the necessity of large working distances to allow for potential bulky equipment at the sample position, we extend the concept of intermediate focus to grazing incidence geometries. This allows for achieving small beam sizes in combination with large working distances at the same time in the hard X-ray region. The employed strategy is based on the use of an intermediate focus between the source and the sample that is subsequently refocused at the sample position. This methodology opens up the use of small micrometric or submicrometric beam sizes in combination with special setups or sample environments

that necessitate large working distances. Moreover, it has been shown that with an adequate selection of the focusing distance for the intermediate focus as well as a convenient distance between the first and second focusing elements it is possible to tune both the beam size and the working distance of the complete optical system to the requirements of the experimental setups. The selected results prove the wide range of applications of this microfocusing methodology, ranging from scanning μSAXS to *in situ* μGISAXS and μGIWAXS.

ACKNOWLEDGMENTS

[1] A. Buffet, A. Rothkirch, R. Döhrmann, V. Körstgens, M. M. A. Kashem, J. Perlich, G. Herzog, M. Schwartzkopf, R. Gehrke, P. Müller-Buschbaum, and S. V. Roth, J. Synchrotron Radiat. **19**, 647 (2012).
[2] C. J. Schaffer, C. M. Palumbiny, M. A. Niedermeier, C. Jendrzejewski, G. Santoro, S. V. Roth, and P. Müller-Buschbaum, Adv. Mater. **25**, 6760 (2013).
[3] S. Yu, G. Santoro, K. Sarkar, B. Dicke, P. Wessels, S. Bommel, R. Döhrmann, J. Perlich, M. Kuhlmann, E. Metwalli, J. F. H. Risch, M. Schwartzkopf, M. Drescher, P. Müller-Buschbaum, and S. V. Roth, J. Phys. Chem. Lett. **4**, 3170 (2013).
[4] J. Perlich, J. Rubeck, S. Botta, R. Gehrke, S. V. Roth, M. A. Ruderer, S. Prams, M. Rawolle, Q. Zhong, V. Körstgens, and P. Müller-Buschbaum, Rev. Sci. Instrum. **81**, 105105 (2010).
[5] N. Tamura, A. A. MacDowell, R. Spolenak, B. C. Valek, J. C. Bravman, W. L. Brown, R. S. Celestre, H. A. Padmore, B. W. Batterman, and J. R. Patel, J. Synchrotron Radiat. **10**, 137 (2003).
[6] M. A. Marcus, A. A. MacDowell, R. Celestre, A. Manceau, T. Miller, H. A. Padmore, and R. E. Sublett, J. Synchrotron Radiat. **11**, 239 (2004).
[7] M. Kunz, N. Tamura, K. Chen, A. A. MacDowell, R. S. Celestre, M. M. Church, S. Fakra, E. E. Domning, J. M. Glossinger, J. L. Kirschman, G. Y. Morrison, D. W. Plate, B. V. Smith, T. Warwick, V. V. Yashchuk, H. A. Padmore, and E. Ustundag, Rev. Sci. Instrum. **80**, 035108 (2009).
[8] P. Müller-Buschbaum, Anal. Bioanal. Chem. **376**, 3 (2003).
[9] A. Snigirev and I. Snigireva, in *Modern Developments in X-Ray and Neutron Optics*, edited by A. Erko, M. Idir, T. Krist, and A. Michette (Springer-Verlag, Berlin, Germany, 2008), p. 255.
[10] A. Guilherme, G. Buzanich, and M. L. Carvalho, Spectrochim. Acta B **77**, 1 (2012).

[11]P. Kirkpatrick and A. V. Baez, J. Opt. Soc. Am. **38**, 766 (1948).

[12]H. Mimura, S. Handa, T. Kimura, H. Yumoto, D. Yamakawa, H. Yokoyama, S. Matsuyama, K. Inagaki, K. Yamamura, Y. Sano, K. Tamasaku, Y. Nishino, M. Yabashi, T. Ishikawa, and K. Yamauchi, Nat. Phys. **6**, 122 (2010).

[13]M. Yanagihara and K. Yamashita, in *X-Ray Spectrometry: Recent Technological Advances*, edited by K. Tsuji, J. Injuk, and R. Van Grieken (John Wiley and Sons Ltd., Chichester, UK, 2004), p. 63.

[14]D. X. Balaic, K. A. Nugent, Z. Barnea, R. Garrett, and S. W. Wilkins, J. Synchrotron Radiat. **2**, 296 (1995).

[15]A. Jarre, C. Fuhse, C. Ollinger, J. Seeger, R. Tucoulou, and T. Salditt, Phys. Rev. Lett. **94**, 074801 (2005).

[16]S. Roth, M. Burghammer, A. Janotta, and C. Riekel, Macromolecules **36**, 1585 (2003).

[17]B. Nöhammer, C. David, M. Burghammer, and C. Riekel, Appl. Phys. Lett. **86**, 163104 (2005).

[18]S. V. Roth, T. Autenrieth, G. Grübel, C. Riekel, M. Burghammer, R. Hengstler, L. Schulz, and P. Müller-Buschbaum, Appl. Phys. Lett. **91**, 091915 (2007).

[19]I. Snigireva, A. Snigirev, V. Kohn, V. Yunkin, M. Grigoriev, S. Kuznetsov, G. Vaughan, and M. Di Michiel, Phys. Status Solidi A **204**, 2817 (2007).

[20]M. Mayer, K. Keskinbora, C. Grevent, A. Szeghalmi, M. Knez, M. Weigand, A. Snigirev, I. Snigireva, and G. Schütz, J. Synchrotron Radiat. **20**, 433 (2013).

[21]H. C. Kang, J. Maser, G. B. Stephenson, C. Liu, R. Conley, A. T. Macrander, and S. Vogt, Phys. Rev. Lett. **96**, 127401 (2006).

[22]H. Yan, V. Rose, D. Shu, E. Lima, H. C. Kang, R. Conley, C. Liu, N. Jahedi, A. T. Macrander, G. B. Stephenson, M. Holt, Y. S. Chu, M. Lu, and J. Maser, Opt. Express **19**, 15069 (2011).

[23]A. Snigirev, V. Kohn, I. Snigireva, and B. Lengeler, Nature (London) **384**, 49 (1996).

[24]C. G. Schroer and B. Lengeler, Phys. Rev. Lett. **94**, 054802 (2005).

[25]B. Lengeler, C. G. Schroer, M. Kuhlmann, B. Benner, T. F. Guenzler, O. Kurapova, F. Zontone, A. Snigirev, and I. Snigireva, J. Phys. D: Appl. Phys. **38**, A218 (2005).

[26]A. Timmann, R. Döhrmann, T. Schubert, H. Schulte-Schrepping, U. Hahn, M. Kuhlmann, R. Gehrke, S. V. Roth, A. Schropp, C. Schroer, and B. Lengeler, Rev. Sci. Instrum. **80**, 046103 (2009).

[27]A. Schropp, R. Hoppe, J. Patommel, D. Samberg, F. Seiboth, S. Stephan, G. Wellenreuther, G. Falkenberg, and C. G. Schroer, Appl. Phys. Lett. **100**, 253112 (2012).

[28]V. Nazmov, E. Reznikova, A. Last, J. Mohr, V. Saile, M. DiMichiel, and J. Gottert, Nucl. Instrum. Methods Phys. Res. A **582**, 120 (2007).

[29]P. van der Linden, H. Vitoux, R. Steinmann, B. Vallone, and C. Ardiccioni, J. Phys.: Conf. Ser. **425**, 012015 (2013).

[30]S. Couet, T. Diederich, K. Schlage, and R. Röhlsberger, Rev. Sci. Instrum. **79**, 093908 (2008).

[31]R. Döhrmann, S. Botta, A. Buffet, G. Santoro, K. Schlage, M. Schwartzkopf, S. Bommel, J. F. H. Risch, R. Mannweiler, S. Brunner, E. Metwalli, P. Müller-Buschbaum, and S. V. Roth, Rev. Sci. Instrum. **84**, 043901 (2013).

[32]M. Schwartzkopf, A. Buffet, V. Körstgens, E. Metwalli, K. Schlage, G. Benecke, J. Perlich, M. Rawolle, A. Rothkirch, B. Heidmann, G. Herzog, P. Müller-Buschbaum, R. Röhlsberger, R. Gehrke, N. Stribeck, and S. V. Roth, Nanoscale **5**, 5053 (2013).

[33]T. Slobodskyy, P. Schroth, D. Grigoriev, A. A. Minkevich, D. Z. Hu, D. Schaadt, and T. Baumbach, Rev. Sci. Instrum. **83**, 105112 (2012).

[34]G. Herzog, M. M. Abul Kashem, G. Benecke, A. Buffet, R. Gehrke, J. Perlich, M. Schwartzkopf, V. Körstgens, R. Meier, M. A. Niedermeier, M. Rawolle, P. Müller-Buschbaum, W. Wurth, and S. V. Roth, Langmuir **28**, 8230 (2012).

[35]V. Körstgens, R. Meier, M. A. Ruderer, S. Guo, H. Y. Chiang, J. Perlich, S. V. Roth, R. Gehrke, and P. Müller-Buschbaum, Rev. Sci. Instrum. **83**, 076107 (2012).

[36]R. J. Davies, M. Burghammer, and C. Riekel, Appl. Phys. Lett. **87**, 264105 (2005).

[37]I. Šics, A. Nogales, T. A. Ezquerra, Z. Denchev, F. J. Baltá-Calleja, and R. Döhrmann, Rev. Sci. Instrum. **71**, 1733 (2000).

[38]D. Sen, O. Spalla, O. Tache, P. Haltebourg, and A. Thill, Langmuir **23**, 4296 (2007).

[39]J. Bahadur, D. Sen, S. Mazumder, B. Paul, A. Khan, and G. Ghosh, J. Colloid Interface Sci. **351**, 357 (2010).

[40]D. Sen, J. Bahadur, S. Mazumder, G. Santoro, S. Yu, and S. V. Roth, Soft Matter **10**, 1621 (2014).

[41]S. S. Hu, J. Rieger, S. V. Roth, R. Gehrke, R. J. Leyrer, and Y. F. Men, Langmuir **25**, 4230 (2009).

[42]X. Chen, V. Boyko, J. Rieger, F. Reinhold, B. Reck, J. Perlich, R. Gehrke, and Y. Men, Soft Matter **8**, 12093 (2012).

[43]M. Kuhlmann, J. M. Feldkamp, J. Patommel, S. V. Roth, A. Timmann, R. Gehrke, P. Müller-Buschbaum, and C. G. Schroer, Langmuir **25**, 7241 (2009).

[44]P. Müller-Buschbaum, D. Magerl, R. Hengstler, J. F. Moulin, V. Körstgens, A. Diethert, J. Perlich, S. V. Roth, M. Burghammer, C. Riekel, M. Gross, F. Varnik, P. Uhlmann, M. Stamm, J. M. Feldkamp, and C. G. Schroer, J. Phys.: Condens. Matter **23**, 184111 (2011).

[45]J. F. Moulin, S. V. Roth, and P. Müller-Buschbaum, Rev. Sci. Instrum. **79**, 015109 (2008).

[46]E. Metwalli, J.-F. Moulin, J. Perlich, W. Wang, A. Diethert, S. V. Roth, and P. Müller-Buschbaum, Langmuir **25**, 11815 (2009).

[47]V. Körstgens, M. Philipp, D. Magerl, M. A. Niedermeier, G. Santoro, S. V. Roth, and P. Müller-Buschbaum, RSC Adv. **4**, 1476 (2014).

[48]N. Sanandaji, L. Ovaskainen, M. Klein Gunnewiek, G. J. Vancso, M. S. Hedenqvist, S. Yu, L. Eriksson, S. V. Roth, and U. W. Gedde, Polymer **54**, 1497 (2013).